Coastal Engineering 61 (2012) 42–48

Contents lists available at SciVerse ScienceDirect

Coastal Engineering

journal homepage: www.elsevier.com/locate/coastaleng

Short communication

A new breaking wave height direct estimator from video imagery

Rafael Almar [a,e,*], Rodrigo Cienfuegos [a], Patricio A. Catalán [b], Hervé Michallet [c], Bruno Castelle [d], Philippe Bonneton [d], Vincent Marieu [d]

[a] Departamento de Ingeniería Hidráulica y Ambiental, Escuela de Ingeniería, Pontificia Universidad Catolica de Chile, Vicuña Mackenna 4860, Macul, Santiago, Chile
[b] Departamento de Obras Civiles, Universidad Técnica Federico Santa Maria, Valparaíso, Chile
[c] CNRS/UJF/G-INP, UMR LEGI, BP53, 38041, Grenoble, France
[d] UMR EPOC (Université Bordeaux 1/CNRS), Bordeaux, France
[e] IRD/UMR LEGOS, Toulouse, France

ARTICLE INFO

Article history:
Received 10 December 2010
Received in revised form 5 December 2011
Accepted 6 December 2011
Available online 29 December 2011

Keywords:
Remote sensing
Wave measurement
Laboratory experiment
Roller
Wave front face angle
Height-to-depth ratio
Coastal management

ABSTRACT

Breaker height is a key parameter of nearshore processes and the demand for a continuous remote estimator is pressing. In this paper we present a standalone remote video-based method that estimates wave height at the breakpoint. Individual breaking events are first identified from changes in optical properties and wave height is further derived from the optical signature at the onset of breaking. An extended validation is performed using a dense wave basin dataset. The results show the ability of the method to measure individual breaker heights (9% of mean error, 18% RMS). In addition, the unique combination of in situ and remotely sensed data allows the estimation of two other breaking-related parameters, the height-to-depth ratio and wave front face slope, which show a substantial amount of dispersion. Because nearshore video systems are rapidly spreading over world coasts, this low-cost remote breaker height estimator should encounter large interest in coastal engineering studies.

1. Introduction

One of the most important parameters for the description and modelling of nearshore hydrodynamics is the wave height and its spatial and temporal distribution. Its variation from deep water to the shore primarily depends on the offshore wave characteristics and the bathymetry over which propagation takes place. Other complex aspects, such as nonlinear effects or wave-current interactions, can also influence wave height evolution in the nearshore (Svendsen, 2006). Due to its complexity, the nearshore wave height remains a difficult parameter to estimate. Moreover, up to now, direct wave measurements are costly, laborious and limited to short term and localized field observations carried out on an energetic and potentially hazardous environment.

Within the scope of the current development of integrated coastal zone management, data assimilation methods based on remotely sensed parameters (e.g. BeachWizard, van Dongeren et al., 2008) have gained support. For instance, standard remote sensing techniques based on optical imagery (video, see Holman and Stanley, 2007 for a review) can produce good estimates of the nearshore bathymetry through depth-inversion algorithms, where wave celerities or a proxy for wave breaking energy dissipation are used as input (Stockdon and Holman, 2000; van Dongeren et al., 2008). Despite the adverse effect of wave nonlinearity on the accuracy of bathymetric estimates in shallow water (Catalán and Haller, 2008) wave height data is either neglected or, at best, deduced from offshore wave gages or numerical models. Regarding the latter, besides requiring an estimated bathymetry, the accuracy of the resulting nearshore wave climates is doubtful over complex bathymetries and under highly energetic conditions (Huntley et al., 2009). Phase averaging models (e.g. SWAN, Booij et al., 1999) are commonly used to propagate wave height (H) from deep water to the shore but this might result in non-negligible errors in the breaker height estimation (H_b) (e.g. Browne et al., 2007) and ultimately in the accuracy of bathymetric assessment using depth-inversion methods.

This emphasizes the need of a local, remotely sensed observation of wave height in the nearshore zone. A remote sensing approach has the potentiality to overcome some of the difficulties typically encountered in the field for energetic wave conditions while providing synoptic measurements with large spatial and long temporal coverage, at affordable operational costs. Moreover, remotely sensed data can provide additional wave information on breaking related parameters such as the location and frequency of occurrence (Aarninkhof et al., 2005; Catalán and Haller, 2008; Haller and Catalán, 2009).

A few studies have attempted estimating wave heights from video-based remote sensing systems. Hilmer (2005) proposed to estimate H_b by rectifying images to a vertical plane, approximating a constant distance between the breakpoint and the camera. The study site was a

* Corresponding author. Tel.: +33 5 61 33 30 06; fax: +33 5 61 25 32 05.
E-mail address: rafael.almar@ird.fr (R. Almar).

0378-3839/$ – see front matter © 2011 Elsevier B.V. All rights reserved.
doi:10.1016/j.coastaleng.2011.12.004

corral reef barrier located 500 m from the camera with wave measurements located in deep water. Other studies computed wave height from a moored pole or buoy in the nearshore (Kim et al., 2008). The horizontal distance between camera and the wave front was thus fixed and only the vertical displacement was considered. Other methods used the position of the breakpoint (x_b) to estimate H_b. Such methods are based on the tracking of the individual breakpoint (Pradal et al., 2002; Yoo et al., 2011) or of the seaward edge of the time-averaged surf zone position (VISSER project, Holland et al., 2002, Huntley et al., 2009). H_b is then estimated using a constant H_b-to-depth ratio as breaking criterion. It can be noted that these methods require a known bathymetry to estimate wave height, which is seldom available. On the other hand, microwave systems have been used to estimate statistical wave height parameters in deep water (Borge et al., 2004), but the applicability to the nearshore has not been demonstrated yet.

In this paper we present a relatively simple method to estimate the location of the breakpoint x_b and the wave height at breaking H_b on a wave-by-wave basis, based solely on video data. Validation is performed using collocated wave measurements from a laboratory experiment.

2. Experimental setup

The laboratory experiment was undertaken in 2008 at the multidirectional basin of the SOGREAH (LHF facility, France; Michallet et al., 2010, Castelle et al., 2010). The basin extent was 30 m in both cross-shore ($X=0$ at the wavemaker) and alongshore ($Y=0$ at the basin border closer to the camera) directions and comprised 60 independently-controlled piston-type wavemakers (Fig. 1a). Free surface displacements were measured at 50 Hz using 18 capacitive gages deployed every 1 m on a movable structure extending in the cross-shore direction. Each experiment consisted of repetitions of 20-min sequences of irregular waves complying with a JONSWAP spectrum. The different runs correspond to the same wave sequence but different long-shore positions of the sliding rail that supports the gages. In this study, we consider two contrasted experiments; experiment 34 with a significant wave height of $H_s=18$ cm at the wavemaker and a peak period $T_p=3.5$ s and experiment 43 with rather short-crested waves $H_s=23$ cm and $T_p=2.3$ s (Fig. 1b).

The bathymetry consisted of a sandy moveable bed resulting in the formation of a nature-like three-dimensional surfzone bar and rip features. In this study, we consider two topographic profiles; one at $Y=18$ m, in a rather monotonic bathymetric area, and a second at a rather barred profile, located at $Y=12$ m (Fig. 1c).

A 720×576-pixel video camera was installed at the basin corner (Fig. 1a). Video grabbed wave-runs at 25 frames per second rate and was post-synchronized with the free surface time series. Rectification of images from pixel coordinates into basin coordinates was accomplished by direct linear transformation using 29 ground survey points (Holland et al., 1997) after a correction of the lens radial distortion. Although varying somewhat throughout the field of view, the cross-shore horizontal footprint was less than 15 cm in the region of interest.

20-minute timestack images were generated at pixels collocated with cross-shore gages. The lighting of this indoor experiment was designed to be diffusive thus allowing identification of the wave trajectory before and after breaking. An illustration of resulting timestack image is shown in Fig. 2a.

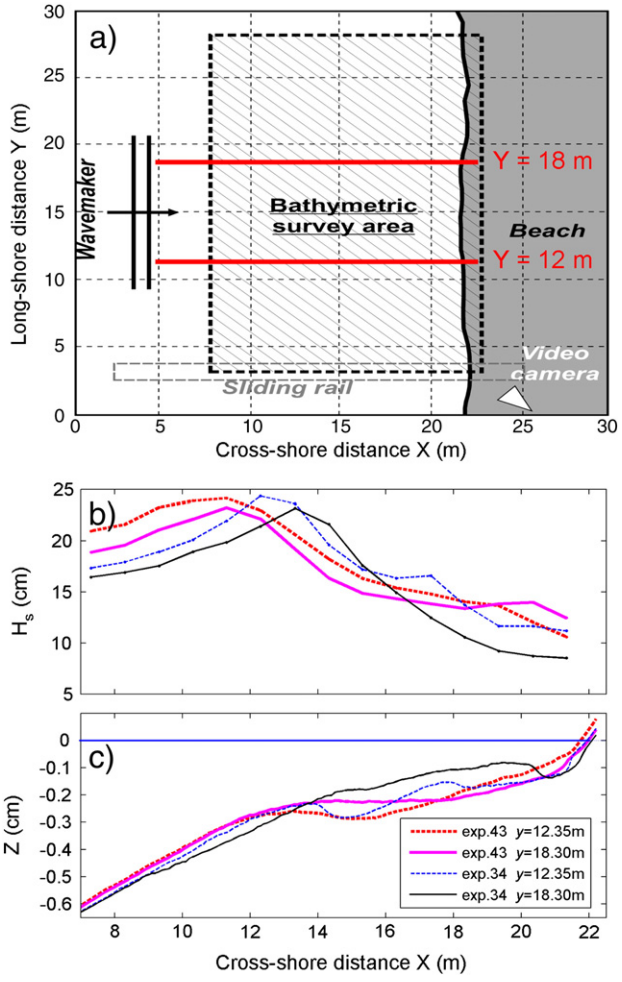

Fig. 1. (a) Schematic diagram of the experimental setup. (b) Cross-shore variation in significant wave height (c) Bathymetric profiles.

3. Method of breaking wave height extraction from video imagery

The method relies on the abrupt change of wave optical characteristics at the breakpoint. Offshore of the breakpoint, the main imaging mechanism corresponds to surface reflections, which are characterized by a narrow dynamic range in optical pixel intensity (Lynch and

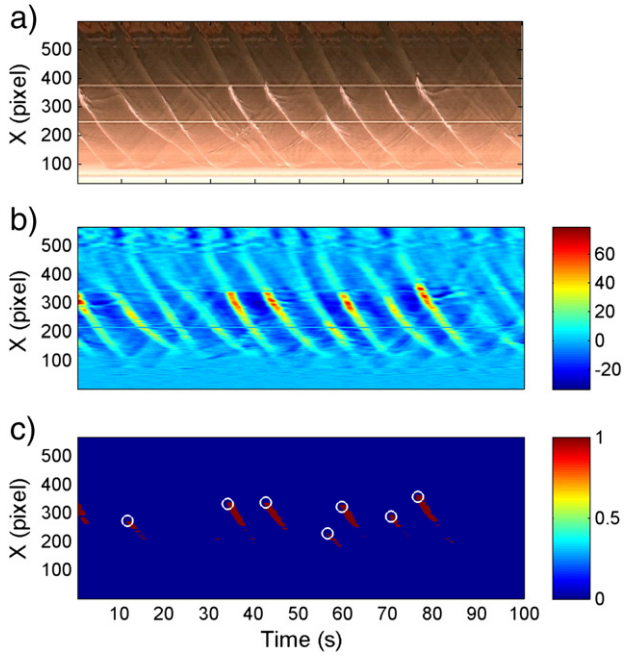

Fig. 2. (a) Raw cross-shore timestack image aligned with the $Y=18$ m profile (cf. Fig. 1). It can be seen the wave's propagation from deep water (up) to the beach (down) over time (from left to right). (b) Resulting time-filtered image. (c) Roller identification (red zones) by application of a pixel intensity threshold. White circles represent the location of identified breakpoints.

Livingston, 1995). Then, as the wave breaks, the turbulent air–water mixture is a source of diffuse reflections. As a result, a large jump in intensity is present when the wave breaks (e.g. Catalán et al., 2011). Therefore, an abrupt change in optical pixel intensity is associated to the onset of breaking and further to H_b on a wave-by-wave basis.

3.1. Determination of the breakpoint position

As seen in Fig. 2a, the wave signature is the dominant structure in the signal, although in the surf zone some spurious signals exist due to remnant foam induced by breaking or other perturbations (e.g. cables, spurious optical reflexions). To minimize their influence on the analysis, the raw timestack image is time-domain filtered around the wave period [T−2 s; T+2 s] using a running average. A sample-filtered image is shown in Fig. 2b. It is worth noting that the period is computed from an offshore pixel intensity timeserie (14% error on the estimated period) using a mean zero-crossing method (Almar et al., 2008).

Next, an intensity threshold is used to discriminate between breaking and non-breaking pixels, similarly to the method described in Catalán and Haller (2008). As the intensity of breaking waves is significantly larger ($I>80$) than that of non-breaking waves ($I\sim10$), the roller contour determination is rather insensitive to the chosen threshold value; a value $I=40$ was applied. Pixels above the threshold are grouped by proximity and associated to individual breaking waves. The results of the discrimination procedure are shown in Fig. 2c. It can be seen that most of the events are well retrieved, although some of the smaller breaking waves are ignored. Finally, the cross-shore breakpoint location, x_b, and the time t_b of the breaking point are given by the coordinates in space and time of the most offshore point of each group.

3.2. Breaker height extraction

Once individual breakpoints are localized, it is possible to extract the local breaker height H_b based on the intensity signal and basic geometrical relations. In order to illustrate the H_b estimation procedure, we show in Fig. 3 the evolution of the intensity signal during the onset of an individual breaking event (Fig. 3a). Fig. 3b represents the cross-shore intensity profile at three different times; prior to breaking, $t_b-0.4$ s, at t_b, and shortly after the breaking has occurred, $t_b+0.4$ s. Prior to breaking ($t_b-0.4$ s), the wave front is associated to weak intensities and a small dynamic range. As breaking initiates (t_b), a clear intensity peak appears at the wave crest. Next, as the roller develops and foam slides toward the wave trough (from t_b to $t_b+0.4$ s), the pixel intensity at the peak increases. As the wave continues to break, the horizontal extension of the intensity peak is no longer only associated to the wave face but to roller propagation and remaining foam. For this reason, breaker height can only be computed at x_b.

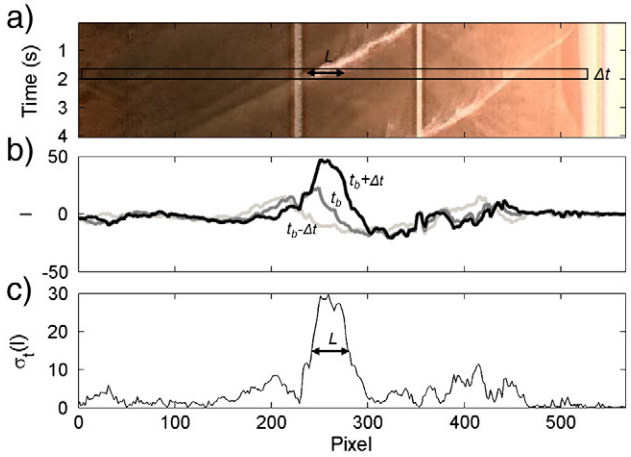

Fig. 3. (a) Timestack image centred on an individual breaking event; the black box represents a 0.4 seconds time window. Waves propagate from left to the right, the beach being located on the right. Related profiles of (b) pixel intensity anomaly I (pass-band time filtered) at successive time steps: $t_1=t_b-0.4$ s, $t_2=t_b$ and $t_3=t_b+0.4$ s. (c) Standard deviation (σ) over the 0.4 s time-window identified in a). L represents the horizontal projection of the wave face covered by the roller.

The estimation of H_b relies on the sudden variation of intensity values associated to breaking inception. For each video-identified breaker, a standard deviation σ of the time series of pixel intensity is computed on a time-window Δt centred on t_b (see the black box in Fig. 3a), thus letting the roller to extend over the wave face. σ measures the intensity variation within Δt and allows to identify the positions where the breaking inception induces a sudden increase of pixel intensity. A time window of $\Delta t=0.4$ s has been chosen based on empirical assessments since most of the different breaking event types encountered during the experiments have been correctly captured. The σ calculated at each cross-shore position shown in Fig. 3c presents a large peak at x_b (around pixel $i=250$, Fig. 3b). This peak is the signature of the white incipient roller while extending on the wave front face at the first moments of breaking. Even if this wave front face is actually inclined, it appears in the video images as projected in a horizontal plan. The width of the peak can thus be associated to the horizontal projection of the wave face covered by the roller (L). L is defined as the width (in pixels) at the half peak. L is further converted into meters unit, knowing the pixel footprint resolution.

Finally, the horizontal distance L is projected into a vertical H_b. This is achieved through simple geometrical relations. A first rough estimation of H_b is obtained from the known camera viewangle (β), assuming that the wave face is vertical:

$$H_b = L\tan\beta \tag{1}$$

However, the fact that wave front slope at breaking (α_b) can differ significantly from vertical should be further taken into account. For example, Govender et al. (2002) estimated using video imaging that plunging waves start breaking for $\alpha_b \approx 30°$. In our methodology, we choose this value commonly used as a breaking criterion in numerical breaking parameterizations (e.g. Cienfuegos et al. 2010). From these considerations, a geometrical correction on L (Fig. 4) is defined as:

$$\mathrm{Cor} = \frac{L}{\tan a_b}\tan\beta \tag{2}$$

Where β is small and can be approximated constant for all individual breakers. In the present case, β is close to 9.5°.

The estimate of H_b in Eq. (1) is then further refined, taking into account the breaker front face slope α_b (see Fig. 4). The latter provides the following relation:

$$H_b = (L-\mathrm{Cor})\tan\beta \tag{3}$$

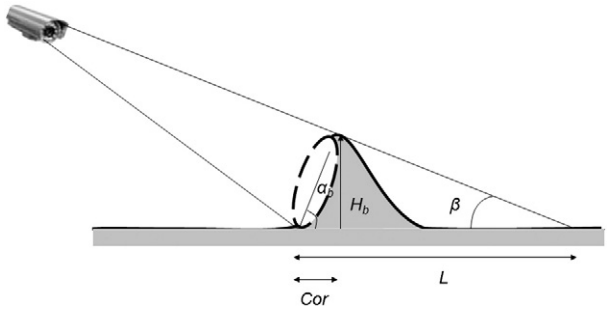

Fig. 4. Scheme of the method principle. Camera viewangle is β and α_b is the wave front face slope. Roller appears as a dashed oval. L is the wave roller horizontal projection, Cor a correction taking into account α_b and H_b is the actual breaker height.

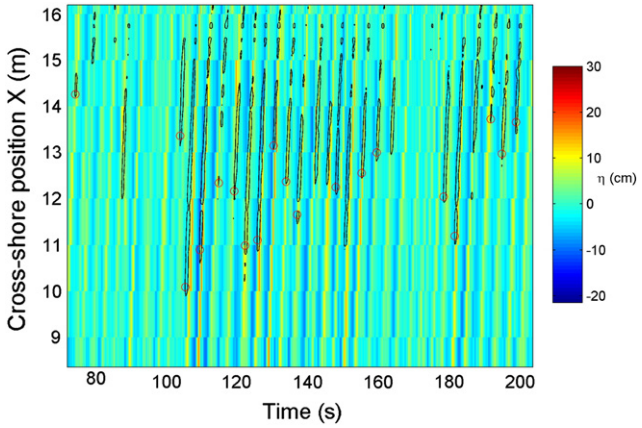

Fig. 5. Superposition of free surface elevation timestack (in cm) with contours denoting the occurrence of wave breaking identified from video data (black). Red circles stand for detected position of video-identified breakpoints.

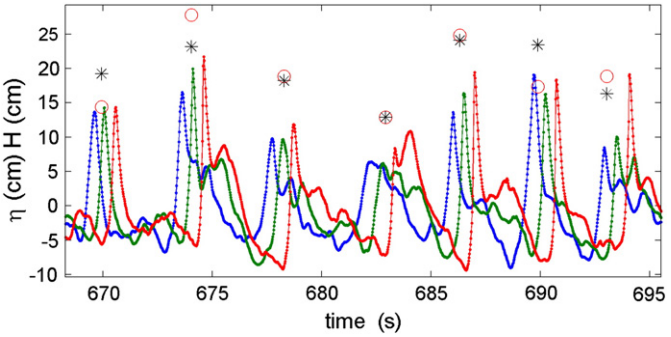

Fig. 7. Timeseries of free surface elevations at $X=11.3$ m (blue), 12.3 m (green) and 13.3 m (red), experiment 34 at $Y=18$ m. Closest (in time and space) video-derived H_b (circles) and gage-derived H_g (stars).

4. Results

The complementarity and consistency of composite in situ-remote data is demonstrated in Fig. 5 where synchronized time series of measured surface elevation and video-derived breaker contours are superimposed. It can be seen that breaking occurs earlier for the largest waves. Using this dense dataset, the video estimator for the breaker height, H_b can be validated at each breaker location x_b, without the need of extrapolating wave height values from distant wave gages as was done previously (Hilmer, 2005; Huntley et al., 2009).

4.1. Validation of our direct H_b video-method estimator

First is validated the performance of the automated algorithm in estimating x_b and L. Automated and manual estimations of both parameters are compared for video-identified breakers of the experiment 34, at $Y=18$ m. From a total of 205 breakers detected, we choose 187 for further consideration, the remainder being disregarded because they represent evident spurious points (e.g. incoherent video signal resulting from beach-reflected waves interference, breakpoint detected too close to the shore due to intermittent breaking). The comparison of automatically- and manually-obtained x_b is presented in Fig. 6a where a very good agreement is observed ($r^2=0.94$). The regression slope value (1.02) indicates the absence of substantial bias. The comparison of L (Fig. 6b) also indicates unbiased values (regression slope close to 1) though data are more scattered in this case ($r^2=0.68$).

The global method performance on H_b estimation is validated next, by comparing for each event, the video-derived H_b against wave height at the closest gage estimated by a zero-crossing method. Time series of free surface elevations from three consecutives gages are plotted in Fig. 7. Video-derived H_b at the closest point, in time and space, are also plotted in the same figure. This allows to determine the closest measured wave height (noted H_g). As shown in Fig. 8, the comparison of video- and gage-derived wave height for both experiments 34 and 43 presents a good consistency, with a total linear regression slope of 0.96 ($r^2=0.43$). The mean and RMS differences are −1.92 cm (i.e. underestimation of video) and 3.9 cm, which represents respectively 9.4% and 18% of gages-derived H_g.

4.2. Video-derived H_b-to-depth ratio and indirect H_b parameterisation

To go into further details, we compare the performances of our direct H_b video-method estimator to a parametric one, previously used in video studies and which necessitates a known depth (Yoo et al., 2011). In this parameterization, H_b is estimated from the local depth, supposing a constant H_b-to-depth (γ_b) value as breaking criterion. γ_b is a crucial parameter because it is commonly used as breaking inception criterion. Numerous observations indicated that γ_b ranges between 0.3 and 1, varying with the Irribarren number (Svendsen, 2006). In our composite in situ-video study, γ_b is estimated by extracting the local

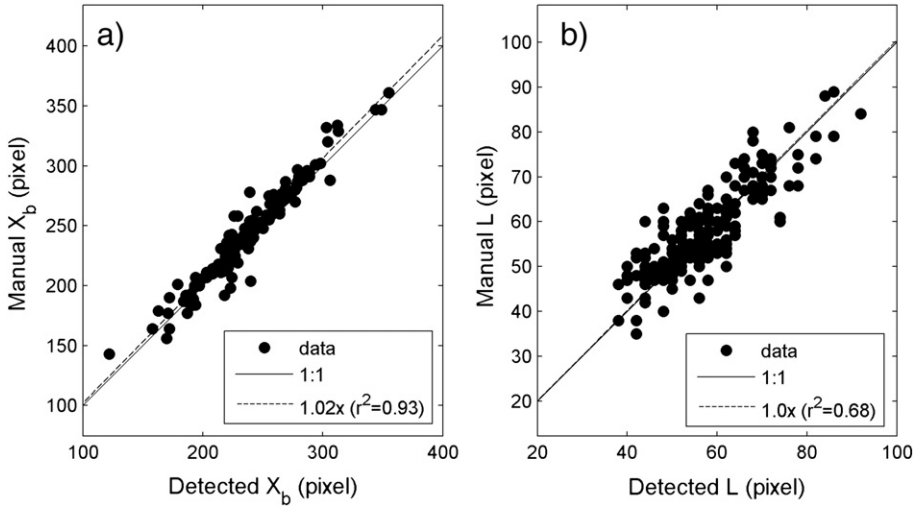

Fig. 6. (a) Comparison of individual breakpoint positions estimated manually (horizontal axis) and automatically (vertical axis). (b) Comparison of breaking inception intensity peak extensions, manually (horizontal axis) and automatically detected (vertical axis).

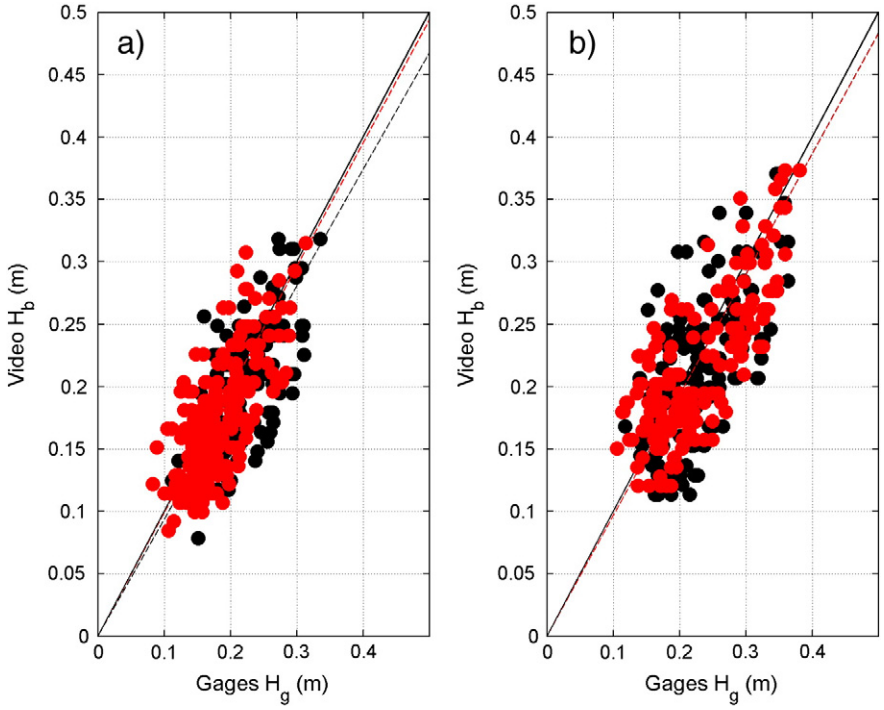

Fig. 8. Video-derived H_b as function of gage-derived H_b at $Y=12$ m (black) and $Y=18$ m (red) for (a) experiment 34 and (b) the experiment 43. Dashed lines are regression lines and solid line is 1:1.

depth and H_b at the video-identified breakpoints (x_b, t_b). γ_b is further applied to a parameterization of H_b.

For two chosen cases were derived the distributions of γ for all passing waves (breaker and non-breakers) at the gage near the breakpoint position ($X=12$ m) (Fig. 9a) and for uniquely the incipient breakers (video-identified at x_b, t_b) (Fig. 9b). It can clearly be seen that γ_b has a limited range of values in comparison with γ. The average γ_b value computed from all video-identified breakers is 0.67. Using $\gamma_b=0.67$, the comparison of the H_b parameterization against measurements indicates a relatively good consistency ($r^2=0.36$), 2.3 cm (11%) and 4.1 cm (19%) for respectively mean and RMS differences. Interestingly, these performances are similar to the ones obtained with our direct H_b video-method estimator that not necessitates information on the underlying bathymetry.

5. Discussion

In contrast with previous H_b predictors from video, our remote estimations were adequately compared to co-localized gages measurements. Although the method's validation holds on laboratory data, it

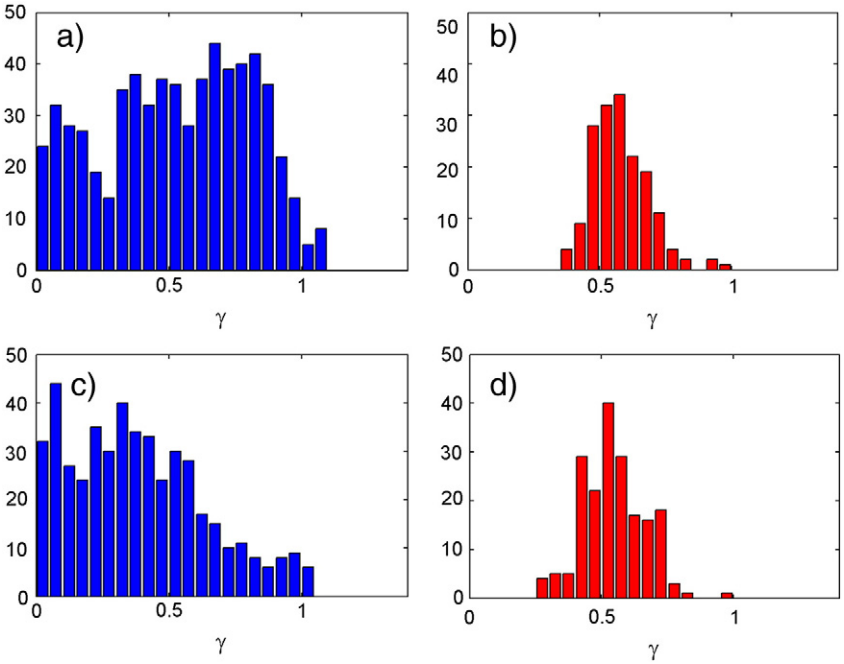

Fig. 9. Distributions of γ computed from all waves (i.e. shoaling waves, breakers and broken waves) passing through a sensor position at $X=12.3$ m (left) and only for breakers (i.e. waves at the breaking point) identified from video for 7 m$<X<$15 m (right); experiment 44 at $Y=18$ m (top) and experiment 34 at $Y=18$ m (bottom).

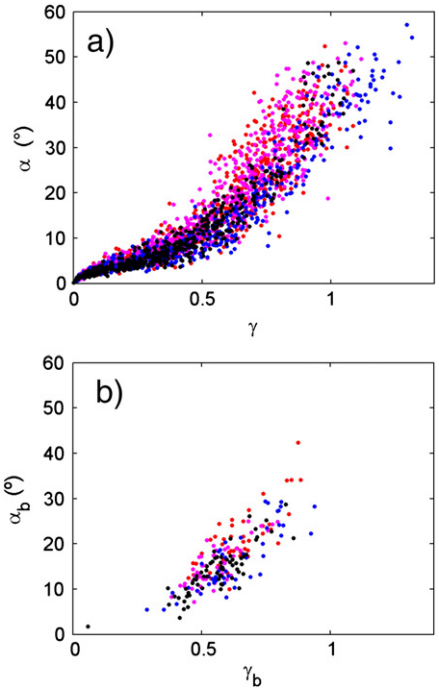

Fig. 10. α as a function of γ for (a) all waves at $X=12$ m and (b) the video-identified breakers in the 7 m<X<15 m zone. Experiment 34 at $Y=12$ m (blue dots), 34 at $Y=18$ m (black), 43 at $Y=12$ m (red) and 43 at $Y=18$ m (pink).

should be readily applied to the field, particularly given the possibility to have diffuse lighting due to overcast skies.

The wave front face slope at breaking α_b is a source of uncertainty for the method. However, a direct estimation of α_b is not an easy task (Duncan, 1981; Govender et al., 2002). From the gage time-series (see Fig. 7), α is computed as the slope (in m/s) of the first 0.1 s ahead of the wave crest divided by the characteristic celerity for surf-zone waves $c=1.2$*sqrt(gh) (Tissier et al., 2011). Noteworthy, c can also be computed from cross-shore arrays of gages. α is plotted as a function of γ for all waves at the mean breakpoint location in Fig. 10a and for video-identified incipient breakers (noted α_b) in Fig. 10b. The correlation between α and γ is good (0.85). As observed between γ and γ_b (see Fig. 9), α_b presents a narrower range of values than α. The average value from all identified breakers is $\alpha_b=23°$. As shown in Fig. 10, α_b has an important wave-to-wave scatter, thus affecting the method-derived H_b estimate which is based on a constant α_b value. From geometrical considerations, this noise effect is higher for small-slope waves.

The second main source of uncertainty in the method comes from the roller inception process. First, it has to be assumed that the roller develops rapidly at the onset of breaking and secondly that it then extends to a constant fraction of the wave front face (R_{frac}). We address the assumption by estimating L on a time-window long enough to let the roller develop completely, roughly one tenth of the wave phase. For the constant R_{frac} assumption, a full coverage can be considered valid as a first approximation for the dataset presented in this paper, from the combination of rather reflective beach and energetic wave conditions (Castelle et al., 2010). However, it might not cope with a softly spilling breaker for which the roller not always fully extends over all the wave faces (Haller and Catalán, 2009). This could cause an underestimation of video-derived H_b when compared to direct measurements.

A sensitivity analysis was performed to help with a rational choice on the couple (α_b, R_{frac}) and to understand their combined influence on the method performance. Mean (Fig. 11a) and RMS (Fig. 11b) errors are computed for varying α_b and R_{frac} values. It is seen that the errors can be minimized for different values of (α_b, R_{frac}). Whereas the blind-approximated combination ($\alpha_b=30°$, full coverage $R_{frac}=1$) applied in this paper gave good results, using the estimate $\alpha_b=24°$ allows an error minimization, if combined to $R_{frac}=0.8$. Plunging breakers are characterized by larger values of both α_b and R_{frac} compared to spilling breakers. This is therefore a further validation of the method that correctly estimates H_b for both plunging and spilling breakers.

It should also be emphasized that, as explained previously, the video breaker-identification process could miss the smallest breakers (weak optical signature due to small footprint) and thus has a tendency to preferentially select larger waves. As a consequence, while compared to gage-derived statistical wave parameters, our dataset-averaged H_b is very close (within a few percents difference) to the significant wave height obtained from gage measurements.

The performances of our direct H_b estimator are similar to those obtained with the H_b parameterization, but without the need of a known bathymetry. This point is crucial and thus of special interest for assimilation and long-term video monitoring systems. Of note, our video wave estimator (H_b, x_b) is now being implemented with success in bathymetric inversion algorithms and video data assimilation schemes (Almar et al., 2011) to account for non-linear wave propagation in the nearshore, reaching an error reduction from linear theory up to 16%.

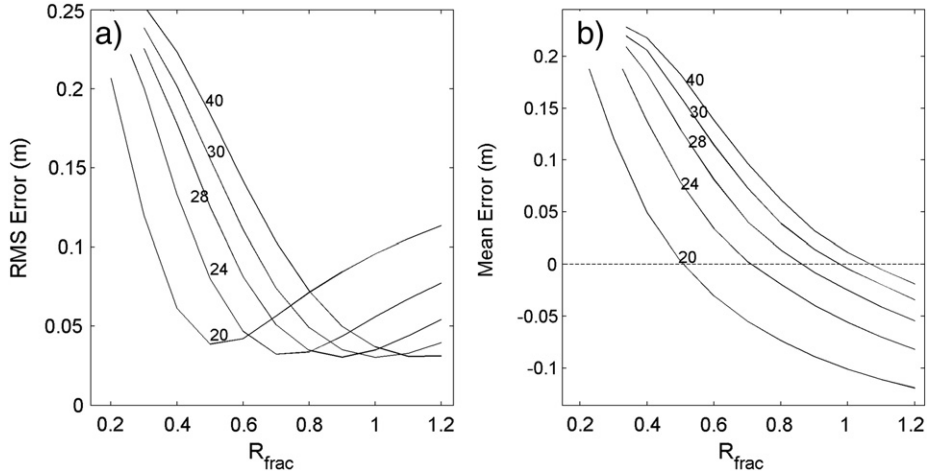

Fig. 11. (a) RMS error and (b) mean error of the method computed from all video-identified breakers as a function of the fraction of the wave face covered by the roller parameter R_{frac} and for various values of α_b from 20° to 40°.

6. Conclusions

This paper presents a standalone direct breaker height estimator from remote video imagery. Optical characteristics of individual waves are processed along cross-shore transects. Breakpoint positions are identified from the sudden variation in optical properties arising from the change of specular (weak intensity) to diffusive reflexion (large intensity). Breaker heights are derived at the breakpoints from the detected extension of incipient rollers on wave faces, assuming a constant breaker slope and a constant fraction of wave face covered by the roller.

A good agreement is found between the automated and manual estimation of breaking optical characteristics, that are, the breakpoint position and roller extension at breakpoint. The comparison of measured and video-derived wave heights at the breakpoint shows a good consistency. Mean and RMS differences represent respectively only 9% and 18% of measured heights, which proves the ability of our video-method to estimate this key parameter. Interestingly, our composite gage-video dataset offers the new possibility of evaluating other breaking-related parameters, such as the breaking wave slope (23°) and height-to-depth ratio (0.68), both showing a substantial variability. These parameters were applied to understand method performance and sources of uncertainty.

This remote, standalone, and low-cost wave height estimator permits to estimate a key parameter and will support new developments in coastal engineering research; particularly within the scope of current strong efforts in data-assimilation and continuous observation.

Acknowledgments

The laboratory work was undertaken within the framework of the Project MODLIT (RELIEFS/INSU, SHOM-DGA). R.A. funded by project FONDECYT No 3110030. B.C. funded by project BARBEC (ANR 2010 JCJC 602 01). H.M. funded by project BARCAN (LEFE/INSU). The first author would also like to thank the post-doctoral fellowship awarded by the Pontificia Universidad Católica de Chile.

References

Aarninkhof, S.G.J., Ruessink, B.G., Roelvink, J.A., 2005. Nearshore subtidal bathymetry from time-exposure video images. Journal of Geophysical Research 110, C06011.

Almar, R., Bonneton, P., Senechal, N., Roelvink, D., 2008. Wave celerity from video imaging: a new method. International Conference on Coastal Engineering 1 (5), 661–673.

Almar, R., Cienfuegos, R., Catalán, P., Birrien, F., Castelle, B., Michallet, H., 2011. Nearshore bathymetric inversion from video using a fully non-linear Boussinesq wave model. Journal of Coastal Research. SI 64 (1), 20–24.

Booij, N., Ris, R.C., Holthuijsen, L.H., 1999. A third-generation wave model for coastal regions: 1. Model description and validation. Journal of Geophysical Research 104, 7649–7666.

Borge, J.N., Rodriguez, G., Hessner, K., Izquierdo, P., 2004. Inversion of marine radar images for surface wave analysis. Journal of Atmospheric and Oceanic Technology 21 (8), 1291–1300.

Browne, M., Castelle, B., Strauss, D., Tomlinson, R.B., Blumenstein, M., Lane, C., 2007. Near-shore swell estimation from a global wind-wave model: spectral process, linear, and artificial neural network models. Coastal Engineering 54, 445–460.

Castelle, B., Michallet, H., Marieu, V., Leckler, F., Dubardier, B., Lambert, A., Berni, C., Bonneton, P., Barthélemy, E., Bouchette, F., 2010. Laboratory experiment on rip current circulations over a moveable bed: drifter measurements. Journal of Geophysical Research 115, C12008. doi:10.1029/2010JC006343.

Catalán, P.A., Haller, M.C., 2008. Remote sensing of breaking wave phase speeds with application to non-linear depth inversions. Coastal Engineering 55, 93–111.

Catalán, P.A., Haller, M.C., Holman, R.A., Plant, W.J., 2011. Optical and microwave detection of surf zone breaking waves. IEEE Transactions on Geosciences and Remote Sensing 49, 1879–1893.

Cienfuegos, R., Barthelemy, E., Bonneton, P., 2010. Wave-breaking model for boussinesq-type equations including roller effects in the mass conservation equation. Journal of Waterway, Port, Coastal, and Ocean Engineering 136 (1), 10–26.

Duncan, J.H., 1981. An experimental investigation of breaking waves produced by a towed hydrofoil. Proceedings of the Royal Society of London. Series A: Mathematical and physical sciences 377, 331–348.

Govender, K., Mocke, G.P., Alport, M.J., 2002. Video-imaged surf zone wave and roller structures and flow fields. Journal of Geophysical Research 107 (C7), 3072.

Haller, M.C., Catalán, P.A., 2009. Remote sensing of wave roller lengths in the laboratory. Journal of Geophysical Research 114, C07022. doi:10.1029/2008JC005185.

Hilmer, 2005. Measuring breaking wave height using video. A senior thesis of the University of Hawai'i.

Holland, K.T., Holman, R.A., Lippmann, T.C., Stanley, J., Plant, N., 1997. Practical use of video imagery in nearshore oceanographic field studies. Oceanic Engineering 22 (1), 81–92.

Holland, et al., 2002. Littoral Environmental Nowcasting System (LENS). Paper Presented at IEEE Oceans Conference.

Holman, R.A., Stanley, J., 2007. The history and technical capabilities of ARGUS. Coastal Engineering 54, 477–491.

Huntley, D.A., Saulter, A., Kingston, K., Holman, R.A., 2009. Use of video imagery to test model predictions of surf heights. Transactions of the Wessex Institute. 12 pp.

Kim, B.O., Cho, H.Y., Lim, D.I., Yoon, G.L., Oh, I.S., Park, Y.A., 2008. Nearshore Wave Measurement Using Single-Video Images of Buoy Motions. Journal of Coastal Research 246, 1481–1486.

Lynch, D.K., Livingston, W., 1995. Color and Light in Nature. Cambridge Univ. Press, New York. pp 245.

Michallet, H., Castelle, B., Bouchette, F., Lambert, A., Berni, C., Barthélemy, E., Bonneton, P., Sous, D., 2010. Modélisation de la morphodynamique d'une plage barrée tridimensionnelle. Actes des XIe Journées Nationales Génie Côtier – Génie Civil (in French), Editions Paralia CFL, Sables d'Olonnes, France, June 2010, pp. 379–386.

Pradal, M.-A., Grilli, S., Dugan, J., Williams, Z., 2002. Application des algorithmes d'inversion de la profondeur à des données de terrain. Actes des VIIe Journées Nationales Génie Côtier – Génie Civil (in French), Anglet, 15–17 Mai 2002.

Stockdon, H.F., Holman, R.A., 2000. Estimation of wave phase speed and nearshore bathymetry from video imagery. Journal of Geophysical Research 105 (C9), 22015–22033.

Svendsen, I.A., 2006. Introduction to nearshore hydrodynamics. : Advanced Series on Ocean Engineering, vol. 24. World Sci.

Tissier, M., Bonneton, P., Almar, R., Castelle, B., Bonneton, N., Nahon, A., 2011. Field measurements and non-linear prediction of wave celerity in the surf zone. European Journal of Mechanics - B/Fluids 30 (6), 635–641. doi:10.1016/j.euromechflu.2010.11.003.

Van Dongeren, A., Plant, N., Cohen, A., Roelvink, J.A., Haller, M.C., Catalán, P.A., 2008. Beach wizard: nearshore bathymetry estimation through assimilation of model computations and remote observations. Coastal Engineering 55, 1016–1027.

Yoo, J., Fritz, H., Haas, K., Work, P., Barnes, C., 2011. Depth Inversion in the Surf Zone with inclusion of wave nonlinearity using video-derived celerity. Journal of Waterway Port, Coastal, and Ocean Engineering 137, 95.